One-Sided Joint Inversion of Shear Velocity and Resistivity from the PI-LAB Experiment at the Equatorial Mid-Atlantic Ridge

Nicholas Harmon[1], Shunguo Wang[2], Catherine Rychert[1], Steven Constable[3], J Michael Kendall[4]

[1] University of Southampton, Ocean and Earth Science, Southampton, UK
[2] Norwegian University of Science and Technology, Trondheim, Norway
[3] University of California, San Diego, Scripps Institution of Oceanography, San Diego, USA
[4] Oxford University, Department of Earth Science Science, Oxford, UK

Abstract

The lithosphere-asthenosphere system is fundamental to our understanding of mantle convection and plate tectonics. Seismic and electromagnetic methods are our primary means of determining its structure and physical properties. These independent constraints with different sensitivities to Earth's properties hold promise for understanding the system. Here we use the shear velocity model from Rayleigh waves and the MT based resistivity model from near the equatorial Mid-Atlantic Ridge. Cross-plots of the models suggest a linear or near-linear trend that is also in agreement with petrophysical predictions. We therefore map the MT model to a new shear-wave starting model using the petrophysical relationship, which is then used to re-invert for shear-wave velocity. The resulting shear-wave velocity model fits the phase velocity data, and the correlation coefficient between the shear velocity and resistivity models is increased. Much of the model can be predicted by expectations for a thermal half-space cooling model, although some regions require a combination of higher temperatures, volatiles, or partial melt. We use the petrophysical predictions to estimate the melt fraction, melt volatile content, and temperature structure of the asthenospheric anomalies. We find up to 4% melt, with the lowest resistivities and shear velocities explained by up to 20% water or 20% CO_2 in the melt or ~1% nearly pure sulfide melt, depending on the set of assumptions used. Melt is required in punctuated anomalies over broad depth ranges, and also in channels at the base of the lithosphere. Melt in the asthenosphere is dynamic, yet persistent on geologic time scales.

Introduction

Plate tectonic theory is predicated on the idea of a rigid lithosphere that overrides a weaker underlying asthenosphere (McKenzie & Parker, 1967), but the nature of the lithosphere-asthenosphere system remains the subject of vigorous debate. The oceanic lithosphere comprises the majority of the surface of the Earth and has the simplest evolution and history. It is classically thought to be thermally defined as a boundary layer in a simple thermal model (Parker & Oldenburg, 1973). In this model, increasing temperature with depth causes mantle rocks to weaken, creating the asthenosphere (e.g.,Goetze et al., 1978). However, a host of observations, including sharp seismic velocity discontinuities (Gaherty et al., 1996; Rychert et al., 2020; Rychert et al., 2018; Rychert & Shearer, 2011; Tan & Helmberger, 2007), low velocity zones (Forsyth et al., 1998; N. Harmon et al., 2020), and low resistivity zones (Baba et al., 2006; Wang et al., 2020) in the asthenosphere, suggest that in addition to temperature other factors are likely required to explain the observations. Many potential explanations of these observations have been proposed including an increased effect of hydration (Karato, 2012), the presence of partial melt (Anderson & Sammis, 1970), and/or the enhanced effects at near sub-solidus conditions on seismic waves (Yamauchi & Takei, 2016). The debate centers around which of these explanations might be in operation and how widely they apply.

Partial melt is likely to exist in the asthenosphere, in particular near mid-ocean ridges and volcanic arcs where the volcanic systems must be fed by mantle melting (Anderson & Sammis, 1970). However, further away from volcanic plate boundaries its presence is more debated (Kawakatsu et al., 2009; Priestley & McKenzie, 2006; Rychert et al., 2005). The amount of melt and its location is vital to our understanding of how the lithosphere-asthenosphere works, as the presence of partial melt is predicted to reduce the viscosity of the asthenosphere (Hirth & Kohlstedt, 1995; Jackson et al., 2006) and could also facilitate plate tectonics (Rychert et al., 2005; Rychert et al., 2007). However, different geophysical techniques with different sensitivities and resolutions have imaged anomalies that have been interpreted as melt in many forms (Rychert et al., 2020). For instance beneath mid-ocean ridges, seismic surface wave studies have interpreted a broad, hundreds of kilometers wide, melt triangle beneath the ultrafast spreading East Pacific Rise at 17 °S (Dunn & Forsyth, 2003; Forsyth et al., 1998) and the intermediate spreading Juan De Fuca Ridge (Bell et al., 2016; Gao, 2016), while other studies have imaged smaller scale and discrete melt zones beneath the slow spreading equatorial Mid-Atlantic Ridges on the order of 100-200 km wide (N Harmon et al., 2020). Magnetotelluric methods have typically imaged smaller and more discrete low resistivity zones interpreted as focused melt regions beneath the fast spreading East Pacific Rise at 9 °N and the ultra-slow spreading Mohns Ridge (Johansen et al., 2019; Key et al., 2013) that are typically < 100 km wide, although a broader region >200 km was inferred beneath the East Pacific Rise at 17 °S (Evans et al., 1999). Further off-axis, layered and/or pervasive melt in the asthenosphere has been inferred based on the imaging of discontinuities by scattered waves that require sharp drops in seismic velocity with depth (Kawakatsu et al., 2009; Rychert & Shearer, 2011; Rychert & Shearer, 2009; Tharimena et al., 2017). Active source seismic studies also find strong reflectors near the expected base of the tectonic plate, that have been interpreted as channelized melt (Mehouachi & Singh, 2018; Stern et al., 2015). Similar channelized structures have also been interpreted from thin low resistivity zones at 60-80 km depth (Naif et al., 2013; Wang et al., 2020). These interpretations are intriguing but originate from methods with a variety of resolutions and sensitivities in different locations. Therefore, whether or not differences are an artefact of resolution and sensitivities of the individual methodologies or representative of real Earth structure has remained unclear.

The complementary resolution and sensitivities of MT and seismic imaging techniques offer a promising means of probing the Earth's physical properties to examine the thermal structure and the presence of partial melt. The Earth's mantle is primarily composed of olivine and pyroxene, and the conductivity of these minerals has a strong temperature dependence (Gardés et al., 2014; Naif et al., 2021), enhanced by the presence of conducting fluids such as partial melt (Naif et al., 2021; Ni et al., 2011) and the presence of water and other crystallographic defects in the olivine mineral lattice (Gardés et al., 2014; Naif et al., 2021). Water and other volatiles such as CO_2 are also thought to significantly increase the conductivity of the fluid and therefore the overall conductivity of the mantle if present (Ni et al., 2011; Sifre et al., 2014). On the other hand, seismic velocities are dependent on temperature and pressure (e.g., Stixrude & Lithgow-Bertelloni, 2005), followed by the presence of partial melt (Clark & Lesher, 2017; Hammond & Humphreys, 2000), particularly for shear velocity, and are relatively insensitive to the presence of water as a crystallographic defect (Abers et al., 2014) or as a component of the partial melt. These differences mean that the two methods together have the potential to better constrain the thermal properties of the mantle, the presence and amount of partial melt, and the amount of hydration in the melt.

There have been two main approaches to joint inversion of electromagnetic and seismic data: 1) inversion based on underlying petrophysical or empirical relationships between velocity and conductivity (Jegen et al., 2009) and 2) inversion based on a cross-gradient approach, e.g. forcing model changes in velocity and resistivity together (Bennington et al., 2015; Gallardo & Meju, 2004; Haber & Oldenburg, 1997; Moorkamp et al., 2011). The petrophysical or empirical approach requires either accurate models of the physical properties of the rocks (Gardés et al., 2014), or ideally a relatively simple system that can be captured with simple linear or polynomial fits to data (Jegen et al., 2009), which is more likely the case in locations with limited compositional and thermal variation. The cross-gradient approach, on the other hand, presumes that low resistivity features should be associated with low or high velocity features, in other words, that the two are positively or negatively correlated. However, this may not necessarily be the case in the presence of small amounts of certain minerals such as magnetite in serpentine (Stesky & Brace, 1973) or graphite (Frost et al., 1989) and other highly conductive minerals which may not be volumetrically significant enough to have a strong seismic signature. Choosing between these two approaches or other approaches using Monte Carlo inversions (Moorkamp et al., 2010) is dependent on the details of the particular datasets and the structure involved.

The I-LAB (Imaging the Lithosphere-Asthenosphere Boundary) experiments including: 1) Passive Imaging of the Lithosphere Asthenosphere Boundary (PI-LAB) experiment, 2) Experiment to Unearth the Rheological Lithosphere-Asthenosphere Boundary (EURO-LAB), and 3) the Central Atlantic Lithosphere-Asthenosphere Boundary (CA-LAB) experiment presented a unique opportunity to examine joint inversion and interpretation of MT and seismic data in order to understand the oceanic lithosphere-asthenosphere system at the equatorial Mid-Atlantic Ridge. We deployed 39 ocean bottom seismometers (OBS) and 39 ocean bottom magnetotelluric (OBMT) instruments from 0-80 Myr seafloor across the Chain and Romanche fracture zones (Agius et al., 2018; Harmon et al., 2018). The OBS and OBMT were co-located (within 1-2 km), in three lines perpendicular to the ridge (Fig. 1). The experiment was designed to image the uppermost mantle beneath the ridge system and examine the evolution of the oceanic lithosphere-asthenosphere system and the nature of the lithosphere-asthenosphere boundary.

Here we focus on two results for joint inversion, the 3-D shear-wave velocity model from Rayleigh wave tomography and the 2-D MT inversion from the two southernmost lines (Fig. 1, 2). The shear velocity model images a high velocity lithosphere, and several punctuated low velocity zones (<4.2 km/s) in the asthenosphere, that were interpreted as melt (N Harmon et al., 2020). Near the ridge axis, asthenospheric low velocity zones are attributed to sub-ridge upwelling (Anomalies A and E in line I and line II, respectively in Fig. 2), while further off-axis the low velocity anomalies are attributed to melting due to upwelling caused by small scale convection (Anomalies B, C, and F in Fig. 2) (N Harmon et al., 2020; Wang et al., 2020). The MT result images similar structures to the surface wave model, e.g., a high resistivity lithospheric lid ($\log_{10}(\rho)$ >2) and several low resistivity anomalies ($\log_{10}(\rho)$ < 1) in the asthenosphere (anomalies A, B, C, D, E, and F in Fig. 2) (Wang et al., 2020). In Line I there is good agreement with the depth (50-80 km) and lateral extent (~100-200 km) of the low resistivity anomaly and low seismic velocities (Anomalies B and C) as well as evidence for a high resistivity, high velocity lithospheric drip (anomaly D) that extended from 50 to 150 km depth. However, in line II (Fig. 2b and 2d) the agreement in terms of the shapes of the anomalies is less remarkable, specifically anomaly F, where the conductive anomalies suggest a channel structure < 20 km thick extending from the ridge to 30 Myr seafloor, while the surface wave anomaly resembles a simple oval ~200 km wide from 50-80 km depth. In addition, anomaly E is deeper in the resistivity model, >100 km depth, than in the shear velocity model, where it extends from 50 to 100 km depth. While in line I, anomaly A is shallower at ~30 km depth and smaller, <50 km wide, in the resistivity model than in the shear velocity model, where it is located at 50-80 km depth and 150 km wide. In other words, while there is some similarity in the lateral locations of the anomalies, the depth and morphologies are a bit different.

Subsequent studies support the existence of these anomalies and suggest that apparent discrepancies may be artefacts of resolution. For example, S-to-P receiver functions support the existence of the anomalies. The receiver functions image discontinuities associated with sharp velocity decreases with depth above the locations of the low shear velocity anomalies E, C, and F in the asthenosphere and also the locations where the low resistivity anomalies gradually decrease with depth in the asthenosphere (near anomaly E and directly beneath F) (Rychert et al., 2021). In addition, a short period Rayleigh wave tomography study, which had better resolution in the upper 60 km than Harmon et al. (2020), imaged a shallower anomaly for anomaly A beneath line I, more consistent with the resistivity model (Saikia et al., 2021). The differences between the surface wave models suggest that there are several possibilities for shear-wave velocity models that will fit the Rayleigh wave data that could also be consistent with the anomaly structure of the resistivity model as well. The primary motivation of this study is to find a satisfactory shear velocity model that is also consistent with structural information from the resistivity models.

Here we jointly consider the Rayleigh wave phase velocities and the MT data to evaluate differences and similarities between the seismic and MT anomaly structures, in particular to determine an Earth structure that can satisfy both datasets within data errors. We compare the models one-to-one to develop an empirical relationship between the two and also consider laboratory-based predictions for shear velocity and resistivity. We use the relationship to translate the MT resistivity to shear-wave velocity and use this as the new starting model for the surface wave tomography inversion. This approach assumes that the structure within the resistivity model is closer to the true earth structure, which may be the case, for example, if a thin channel structure exists, which surface waves would not be able to resolve without prior knowledge. We evaluate the validity of this assumption. Finally, we compare to petrophysical predictions for Earth properties to constrain temperature, the amount of partial melt, and the amount of hydration, carbonization or sulfide weight percentage of the partial melt in the asthenosphere.

Methods

MT data were inverted by Wang et al. (2020), which we briefly summarize here. The determinant of the MT impedance tensor was used to invert logarithmic apparent resistivity and linear phase along two wo-dimensional transects (line I and line II). The approach was chosen to minimize strong 3-D coast effects from the nearby African Coast (Wang et al., 2019). Forward calculations and inversion were performed using the MAR2DEM code (Key, 2016), modified to accept determinant data as an input (Wang et al., 2021). Inversion of MT data with this approach is less dependent on the starting model than surface wave inversion due to the diffusive nature of electromagnetic fields and the smoothness and regularization of the inversion problem. So here we focus on varying the starting model for shear velocity inversion based on structural information from the resistivity data, but not vice versa. We refer to this as a “one-sided” joint inversion.

We first establish a relationship between shear velocity and resistivity in our study area. We use two transects through the three-dimensional shear-wave velocity model of Harmon et al., (2020) in the same locations of the two two-dimensional resistivity model transects of Wang et al., (2020). We make cross-plots separately for the two lines. Cross-plots of the data suggest a linear relationship between the two data sets, but with scatter (Fig. 3). The correlation coefficients of these cross-plots for line I is 0.43 and line II 0.39. A linear regression of line I between shear-wave velocity (km/s) and resistivity ($\log_{10}(\rho)$) with the highest correlation coefficient, yields a solution of $Vs=4.19+0.10*\log_{10}(\rho)$. We did not fit a line to line 2 given the lower correlation and the fact that a linear relationship is less apparent. We also consider predictions from laboratory petrophysical relationships between shear velocity and resistivity for a half-space cooling model with a mantle potential temperature of 1350 °C from 0-40 Myr, the approximate range in of ages along lines I and II (Fig. 4). To model the predicted shear velocity for a given temperature, pressure, and melt fraction we use the Very Broadband Rheology calculator (Havlin et al., 2021), assuming a peridotite mantle composition. We use the attenuation parameterization of (Jackson & Faul, 2010) that is included in the calculator and use an average across the surface wave frequency range used here. In this model, the addition of melt primarily affects shear velocity with ~2-4% velocity reduction for 1% melt volume fraction depending on the dihedral angle (Takei, 1998). The model of Takei (1998) assumes that melt is interconnected, without necessarily proscribing a melt geometry. The associated predicted velocity reduction depends on wetness, which is a measure of the amount of grain to grain contact relative to the melt (Takei, 1998). Other models for the effect of melt on velocity exist based on different assumptions of melt geometry (Clark & Lesher, 2017; Hammond & Humphreys, 2000; Schmeling, 1985) which we evaluate in the discussion section. For resistivity we use the relationship for hydrated mantle peridotite (Gardés et al., 2014) and a model for the conductivity of hydrous mantle melts (Ni et al., 2011). We then use the Hashin-Shtrikman upper bound to calculate the total resistivity of a melt bearing peridotite mantle (Ni et al., 2011). The predictions for an example case with 100 ppm water content in the background mantle and 1% melt in the melt triangle and variable amounts of water in the melt from 4-20 weight % are shown in Figure 4. We perform a linear regression on the melt-free mantle data points (black dots, Fig. 4), and find a relationship of $V_s = 4.14 + 0.11*\log_{10}(\rho)$. This relationship is very similar to the one derived for the cross-plot in line I, but the velocity intercept is 0.05 km/s lower than in our cross-plot, and the slope is only 0.01 km/s/ $\log_{10}(\rho)$ higher than in the cross-plot. Given the similarity between the two and that the petrophysical line visually fits the data from the shear velocity and resistivity inversions, we opt to use the relationship from the petrophysical modelling.

We use the aforementioned petrophysical relationship to translate the resistivity model (Fig. 2a, b) to shear-wave velocity, creating a new starting model (Fig. 5c, d) for the shear velocity inversion. We then invert the phase velocities from 18-143 s period from Harmon et al. (2020) sampled along lines I and II, for shear velocity as a function of depth, sampling at every point, 0.1 °. We calculate the partial derivatives relating Rayleigh wave phase velocity to shear velocity using the Computer Programs in Seismology package (Herrmann, 2013), and we assume a fixed Vp/Vs ratio of 1.8, which is consistent with the Preliminary Earth Reference Model (PREM), a global 1-D seismic velocity model (Dziewonski & Anderson, 1981). We include a seawater layer along lines I and II in the model based on the local bathymetry. We use a damped least-squares inversion and assume an *a priori* model error of 0.2 km/s following choices from previous work (Forsyth & Li, 2005; N Harmon et al., 2020). We replace the upper 5 km of the model beneath the water layer with average crustal values (3.5 km/s) from the 1-D model of Harmon et al. (2020). The model is parameterized every 5 km in depth down to 400 km. This parameterization is finer than that presented in Harmon et al. (2020) (Fig. 2). Therefore, we also present an inversion using the 1-D model used in Harmon et al. (2020), but with the 5 km thick layers down to 400 km depth used here for comparison purposes (Fig. 5).

We next determine the physical properties that explain the resulting anomalies. We calculate the thermal structure for seafloor from 0 to 40 Myr age in 1 Myr intervals. The thermal models have an adiabatic gradient added to them, and we assume a mantle potential temperature of 1350 °C. Although seafloor age is known at each profile, we do not proscribe age, given that our previously published models suggest that the age progression of the lithosphere might not be monotonic everywhere. For each thermal structure from 0 to 40 Myr seafloor, we calculate the predicted shear velocity and resistivity for melt fractions from 0.00 to 0.07 at 0.001 increments below 0.01 and 0.005 increment above 0.01 and melt water contents from 0 to 30 weight % in 1% increments for all temperatures > 1100 °C at the corresponding depth/pressure values using the relationships described above for the half-space cooling model presented in Fig 4. We then examine the regions that cannot be explained by temperature alone, specifically, where the shear velocity is <4.4 km/s and $\log_{10}$ resistivity is < 1.5 (< 30 Ωm), which are the nominal limits of the melt free predictions of the half-space cooling model (black dots, Fig 4). We perform a grid search over melt fraction, melt water content, and apparent seafloor age/temperature for each point in lines I and II. We then determine the chi-squared residual between the observed resistivity and shear velocity with the predicted resistivity and shear velocity at the same depth in each thermal structure from 0 to 40 Myr. The chi-squared residual is used to determine goodness of fit assuming an *a priori* standard deviation of 0.05 km/s for the shear velocity model and 0.10 $\log_{10}(\Omega m)$ for the resistivity model. A value of melt, melt hydration and temperature is considered acceptable if the chi-squared value is < 1 for both the shear velocity and resistivity data. The optimum value is the minimum summed value of the chi-squared values for resistivity and shear velocity. We present the error as the maximum value minus the minimum acceptable value divided by 2 for melt, melt water content and temperature, which is the 95% confidence limit assuming symmetric error surfaces. We acknowledge that this choice of reporting does not give a sense of the trade-offs in these parameters.

Results

The shear-wave velocity structure derived from translating the MT models to seismic velocity according to the petrophysical predictions (Fig. 5c, d) closely resembles the MT models (Fig. 2 a, b), which is to be expected. We impose a water layer of 0.0 km/s in the model, which results in the white area near the top of the model. The seismic velocities range from 4.5 km/s in the upper 20-50 km of the Earth, with a minimum of 4.03 km/s associated with the lowest resistivity regions. Strong lateral gradients are also visible in the starting model, with changes of 0.4 km/s over less than 50 km, particularly near anomaly C. The line II model has low velocity channels across the transect at 20-70 km depth and several high velocity regions in the asthenospheric mantle.

When we use the shear-velocity model derived from MT (Fig. 5c, d) as the starting model for the surface wave inversion we find a new shear-wave velocity model (Fig. 5 e, f) that more closely resembles the MT models than the previously published model (Fig. 2). The highest velocities are up to 4.81 km/s found in the fast lid, while the minimum velocity is 4.00 km/s, found in anomaly B. The high velocity lid is more continuous than in the starting model but follows a similar pattern of increasing thickness away from the ridges in both lines I and II. In the asthenosphere, low velocity structures from the starting model are also retained. Specifically, the channel structures in line II, anomaly E and F, are retained throughout much of the model, particularly in the east near anomaly F, with similar velocities (~4.0 km/s). In line I anomalies B and C are preserved i.e., ~4.0 km/s from the starting model. Anomaly A is more pervasive beneath the ridge than in the MT starting model. Anomaly D is also enhanced in the shear velocity model, with a high velocity of 4.56 km/s relative to the starting model of 4.31 km/s at 100 km depth. The chi-squared values indicating goodness of fit to the data is shown in Fig. 5a and 5b and are ~1 or less for most of the profile indicating a fit this is within error. This goodness of fit is similar to the values from Harmon et al. (2020).

When we use the 1-D starting model from Harmon et al. (2020) for the surface wave inversion, and the parameterisation and damping used here we find similarities and also differences in comparison to Harmon et al. (2020) that illustrate the range of possible models that fit the data (Fig. 5g, h). A high velocity lid is visible beneath the ridge and across the region that ranges from 20-60 km in thickness. It shows low velocities beneath the ridge, with a stronger and shallower low velocity region beneath the ridge than in the model of Harmon et al. (2020), although in general the features are similar and the velocity anomalies are similar < 4.2 km/s but > 4.0 km/s. The normalized chi-squared fit to the data is shown in Fig. 5 a,b for Line I and II, respectively. The chi-squared values are generally ~1 or less indicating that the model fits the data within error and have a similar fit to the model with the MT starting model. The new shear-velocity model with 1-D starting model presented in Figure 5g, h is primarily for demonstrative purposes. The goal of the paper is to align the previously published shear-wave velocity and resistivity models, and so we do not discuss the model of Figure 5g, h further except for the purposes of resolution discussions.

The correlation between resistivity and shear-velocity is higher when the MT derived starting model is used in comparison to when the 1-D starting model is used in the shear-velocity inversion. For the 1-D starting model, there is a slope visible in line I (Fig. 6a), but there is less of a visible relationship in line II (Fig 6b). Visually, the cross-plots for the MT derived starting model are more linear, with more of a slope visible in both lines I and II (Fig. 6 c, d). The correlation coefficients between the resistivity model and the shear velocity model assuming 1-D start model presented here are 0.41 and 0.29 for lines I and II, in other words similar to that between the resistivity and the original shear velocity model presented in Harmon 2020 above (0.43 and 0.39 respectively). The correlation coefficients are higher, 0.56 and 0.62 for lines I and II respectively shear-wave model resulting from the MT-derived starting model. With the two lines combined the correlation coefficient is 0.60 (Fig. 7).

We illustrate the behaviour of the effect of varying the amounts of melt and water in the partial melt and compare it to the V_s and resistivity histogram for both line I and II (Fig. 7). We use the thermal structure from the half-space cooling model shown in Fig. 4 but now allow partial melt at 0.1%, 1.0% and 3.0% where the mantle temperature exceeds 1100 °C. We also vary the amount water in the partial melt between 4-20%. The smallest amount of partial melt reduces the seismic velocity by << 1% in most cases, while the resistivity is reduced by ~0.6 $\log_{10}(\Omega m)$ over the range of water contents presented here. At 1% melt the shear velocity is reduced by ~2%, and the effect of increased water content is stronger, reducing the resistivity up to ~1.5 $\log_{10}(\Omega m)$ at the highest water contents. Finally, at 3% melt, the velocity is reduced by 4-5% and the resistivity reduction is up to ~2.1 $\log_{10}(\Omega m)$. The span of partial melt and melt water contents considered here also generally spans the range of most of the Vs/resistivity modelled values from our inversions, i.e., the petrophysical values overlie the peak in the histogram. There is a slight bias in the seismic velocities with a longer tail towards higher values.

Given the good general agreement between the petrophysical modelling and the shear velocity and resistivity model values, we map the amount of partial melt, water content of the melt, and temperature relative to the half-space cooling model onto the transects of lines I and II (Fig. 8). We only perform this mapping where shear velocity is < 4.4 km/s and $\log_{10}(\rho)$ < 1.5 $\log_{10}(\Omega m)$, which is the nominal lower limit of the melt free half-space cooling model (Fig. 4 and Fig. 7). In line I we find partial melt contents up to 4-4.5% near anomalies B and C and similar maximum values in line II for anomalies E and F. Lower values of partial melt <2% are needed near anomaly A and for most of the other regions, typically requiring < 1%. The water content of the melts is typically < 10 weight % for most (~60 %) of the total anomaly area (colored regions in Fig. 8), with the notable exception of anomaly C which requires up to 24 weight % water content to account for the low resistivity found in this region and anomaly B which requires up to 15 weight %. There are other smaller patches of high-water content visible near the edges of some of the regions, and within the channel of anomaly E. The temperature structure generally has cooler temperatures 1100-1200 °C at depths < 100 km and temperatures > 1300 °C at greater depth. The grid search allows us to assign error bounds corresponding to our presumed data errors (Fig. 9). The errors for the melt percentages are typically <1%, while error for water content of the melt is on average 4 weight %, and the average errors for temperature are 26 °C.

Discussion

Our linear relationship between shear velocity and resistivity produced a reasonable starting model for the shear-wave velocity inversion from Rayleigh waves. The inversion with the MT-derived starting model was able to fit the phase velocity data within error for most of the two profiles shown here and fit the data as well as the 1-D model and the work of Harmon et al., (2020). The MT-derived shear-velocity model improved the visual agreement and correlation coefficient between the resistivity and shear velocity model.

Overall, many of the in common features of the original works are retained and several of the anomalies come into better agreement. For example, the MT-derived shear velocity model retains the thickening of the lithosphere and the drip feature at anomaly D observed in the Harmon et al. (2020) model. The lithospheric thickening with distance from the ridge is more pronounced in the MT-derived shear velocity model in comparison to that of Harmon et al. (2020). Anomalies B and C are also retained in the MT-derived model, although anomaly B is more prominent than in the Harmon et al., (2020). In the asthenosphere, better agreement between the resistivity model and the MT-derived shear velocity model is achieved for the channel features in line II associated with anomaly F. Anomaly C in the MT-derived shear velocity model has a morphology more similar to the MT model than in the Harmon et al., (2020) model. Other anomalies such anomaly A shifts shallower than the Harmon et al., (2020) model, and aligns better with a weak shallow anomaly directly beneath the ridge in the resistivity model. Anomaly E is deeper than that in the Harmon et al. (2020) model, again in better agreement with the resistivity model.

The differences in the shear velocity models here highlight some of the limitations of the approach. Specifically, inversion of Rayleigh wave phase velocities for shear velocity structure is non-unique, and this is well-known (Rychert et al., 2020) as many previous works have demonstrated that a variety of models can fit a given dispersion curve. The differences between Harmon et al. (2020) (Fig. 2), the 1-D starting model with smoothing, damping, and parameterization of this study (Fig. 5e, f) and the MT-derived starting model (Fig. 5g, h) illustrate this fact again and highlight that the strength of an anomaly can vary from model to model depending on the starting model, even if similar damping is used and same fit is achieved as was the case here. For instance, the MT-derived shear-wave velocity model includes velocities in Anomalies B, C by up to 1% slower in comparison with Harmon et al. (2020), which impacts interpretation in terms of the presence of partial melt. Suitable additional constraints are needed to determine which structure is the most likely, such as information from receiver functions or resistivity.

The cross-plots indicate that the shear-wave velocity model and resistivity are in good agreement with the petrophysics predictions for the half-space cooling model and variable partial melt concentrations and melt water contents. About 80% of the shear velocity data lie within 0.1 km/s of the petrophysical predictions for reasonable temperature structure, melt and melt water contents (Fig. 7). The resistivity model is completely spanned by the petrophysical predictions. Shear velocity appears to be biased towards higher values, which may be a result of either the inversion process or a physical process. Shear-wave velocity inversions can trade off velocities at shallow depths with deeper asthenospheric anomalies, by compensating low asthenospheric values with higher lithospheric values. On the other hand, other physical effects such as depletion (Schutt & Lesher, 2006) of peridotite through ridge melting toward more harzburgitic compositions (Hacker & Abers, 2004) could cause higher velocities by ~1-2%. In addition, anisotropy could also enhance the apparent velocity by up to 1-3% (Rychert & Harmon, 2017; Saikia et al., 2021). In reality, it is likely some combination of these physical effects which are not accounted for in the calculations used for predicting shear velocities.

In this work we chose to force the shear velocity structure towards a closer match to the resistivity model, because the MT method has better resolution for certain features such as thin channels, which is an assumption that is worth examination. We presumed the resistivity model has better structural resolution, but this assumption has limitations, since the 2-D assumption for the resistivity model may break down. For instance, anomaly E is part of a larger 3-D anomaly visible that extends to the south along the Mid-Atlantic Ridge in Harmon et al. (2020), and the depth of the anomaly is much greater in the resistivity anomaly, perhaps owing to issues of dimensionality. Other observations, such as S-to-p receiver functions, suggest there may be a shallower shear velocity anomaly associated with anomaly E, which is necessary in order to produce a sharp velocity contrast in these regions (Rychert et al., 2019). However, given that we prefer the MT-derived shear-wave velocity structure for some of the major anomalies (A, B, C, D, and F), we proceed interpreting our estimates for mantle melting and melt water content, bearing the limitations of the inversions in mind.

The thermal structure predicted from our grid search (Fig. 8e, f) suggests relatively warm temperatures beneath Anomalies B and C as well as the deeper parts of E (>1300 °C), while Anomalies A and F have relatively low temperatures (1100-1200°C). This variability is likely a result of the pressure dependence of the seismic waves. The low temperatures are generally consistent with the interpretation that the shallow anomalies, particularly the channel structures in F, are interacting with the base of the lithosphere (N Harmon et al., 2020; Wang et al., 2020). The deeper, hotter anomalies (anomaly B and C) are also generally consistent with the interpretation of upwelling from depth associated with small scale convection.

The predicted melt fractions are in general agreement with our previous work from the region, taking into account the various assumptions. Our melt fraction of up to 0.04 agrees with the 0.01 – 0.07 previously reported based on the resistivity model alone (Wang et al., 2020). It is higher than the 0.005 to 0.015 reported by the previous shear-wave velocity model (N Harmon et al., 2020). However, this can be explained by two main differences: 1) The anomalies in the new shear velocity model presented here are up to 1 % slower than those of the previous study (Harmon et al., 2020) and 2) We used the Takei, (1998) relationship between melt and velocity here, which corresponds to about a 2 % velocity reduction for 0.01 melt fraction in comparison to the 7.9% reduction for 0.01 melt fraction from the work of (Hammond & Humphreys, 2000) used by Harmon et al. (2020). Our melt fraction result of up to 0.04 is also consistent with the 6 – 11 % velocity drop with depth velocity reduction required by receiver functions after correcting for the maximum effect of temperature (Rychert et al., 2021), which would require melt fractions of 0.03 – 0.06 assuming the same melt-velocity relationship from Takei (1998) that we used here.

A different parameterization choice for the effects of melt on velocity due to different assumptions on the melt geometry could yield lower melt fraction requirements by the seismic constraints and still satisfy the resistivity model. Unconnected melt geometries such as for isolated pockets or tubes (Schmeling, 1985) do not affect resistivity and so we can rule those out (Naif et al., 2021). Assuming interconnected films and organized cuspate tubules (Hammond & Humphreys, 2000), as used in Harmon et al., (2020), reduces the maximum amount of partial melt fraction to < 0.02. Melt in the form of interconnected tubules and cuspate geometries (Hammond & Humphreys, 2000), which have a velocity reduction of 14.5% per 0.01 melt fraction would suggest even lower melt fractions (< 0.01). Resistivity does not depend on melt geometry. This is mostly due to the fact that the greatest resistivity reduction occurs at melt fractions < 0.03, with a more gradual reduction in resistivity at higher melt fractions (Fig. 10). However, since resistivity also has a strong dependence on the volatile content in the melt, the lower melt fractions predicted for the interconnected tubules and cuspate geometries could also satisfy the resistivity anomalies with additional volatiles. More work would be required to determine the most likely partial melt geometry and relationship for shear velocity reduction place better constraints on the 3-fold variation predicted from differing assumptions.

Predicted water contents are typically < 10 weight % for the melt but are surprisingly high, up to weight 24%, in the centers of anomaly C, and F. Simple fractional or batch melting calculations suggest that for a typical MORB mantle source with 100 ppm and an average 6% melting of the mantle suggest water contents of the melt should be ~0.2 weight % (Workman & Hart, 2005). Higher water melt contents are possible for low degrees of partial melting, for example <0.005 melt fraction yields > 1% weight water for 100 ppm in the mantle source, and >7% weight water for 800 ppm in the mantle source. One possible explanation is that these off-axis anomalies represent coalesced low-degree melts of a moderately wet mantle with high water content. There is some geochemical evidence for a moderately wet mantle from basalts collected from the ridge segments in the study area, with estimated water contents that range from 110-770 ppm (~ 0.01-0.08 weight %) for the mantle source (Le Voyer et al., 2015). The advantage of this model is that wet melts are stable and can persist in the mantle for long periods of time (Mehouachi & Singh, 2018).

High CO_2 in the mantle melts is another possible explanation for the low resistivities observed in region (Sifre et al., 2014), i.e., instead of high-water contents. Carbonated peridotite is thought to exist in the mantle, although the abundance of carbon is relatively low, likely < 100 ppm, as it is present in ancillary phases, rather than being hosted in olivine or pyroxene (Dasgupta & Hirschmann, 2010). Carbonated melts are generated and stable at greater depths, and only small degrees of partial melt are likely to be generated (<0.001 melt fraction) (Dasgupta & Hirschmann, 2010; Hirschmann, 2010). However, the melts could percolate upwards and coalesce generating higher CO_2 contents in the melt (Hirschmann, 2010). Fig. 10 shows the trade off in effective resistivity for 1 weight % water in the melt, and 10% and 30% CO_2 by weight in the melt as a function of disequilibrium melt fraction assuming 100 ppm in the un-melted mantle background for a depth of 80 km and a temperature of 1350 °C. The figure is for demonstrative purposes since, melt fraction is imposed rather than generated using batch melting or fractional melting, we did not vary temperature as we did in the silicate case, and the melt may not necessarily be stable. At 30% CO_2 weight percent the resistivity is similar to the high-water content (20 weight %) case. However, geochemical estimates of CO_2 in the primary ridge basalts range from 104 ppm to 1.9 weight % (Le Voyer et al., 2019), which is much lower than the >30 CO_2 weight % needed to explain our results. To reach our high values, again aggregation of extremely low degree partial melts would be required, and this also cannot be the melt that directly erupts at the ridge.

Another possible explanation for the observed anomalies besides high water contents (>10%) is sulfide melts, which are extremely conductive, >10^4 S/m (Ducea & Park, 2000). Small amounts of sulfide melts can rapidly reduce the effective resistivity of the aggregate. To illustrate this we follow the parameterization of Ducea and Park (Ducea & Park, 2000), using the (Gardés et al., 2014) parameterizations for the solid olivine and the Ni et al., (2011) parameterization for the silicate melt. We assume a conductivity of 10^4 S/m. Fig. 10 shows a comparison between the effective resistivity for an olivine matrix with wet disequilibrium melts and also for sulfide/wet disequilibrium melt mixtures with predominately sulfide melt. Like the CO_2 case, this is for demonstrative purposes, without varying a full suite of parameters. A nearly pure sulfide melt has a similar resistivity as a silicate melt with 20% water, reaching values below 1 Ωm at < 0.01 melt fraction. So, in this case, regions of high melt water contents in Fig. 8, e.g., anomaly C, could also be regions of high sulfide melt content. Given the bulk abundance of sulphur measured in basaltic glasses in the region typically < 0.1 weight % (Le Voyer et al., 2015) and in <0.3 weight % in xenoliths from continents (Ducea & Park, 2000), it is unlikely that 0.04-0.05 sulfide melt fraction exists in the mantle. However, a more conservative sulfide melt fraction of ~0.01 could at least partially explain anomaly C (Hammond & Humphreys, 2000). There is also some evidence that melts from the nearby ridge segments are sulphur saturated (Le Voyer et al., 2015), and this may therefore suggest that sulfide melts may exist in higher abundance away from the ridge melt triangle where silicate melts are in high abundance. Sulfide melts have also been proposed to explain low seismic wave speeds in the asthenosphere (Helffrich et al., 2011). Further work is needed to test whether sulfide melts would be compatible with small scale convection and explain our off-axis anomalies, as they have a higher density than silicate melts.

The melt anomalies inferred here extend to the base of our well-resolved region, ~150 km depth, which is greater than the 60 – 80 km predictions of a dry melting curve (Katz et al., 2003). This suggests that water or CO_2 induced melting is occurring at depth or the presence of sulfide melts or some combinations are active to produce melts so deep. In addition, the largest melt fractions are associated with anomalies B, C, E and F, which are far from the ridge axis. This suggests melt generation occurs away from the ridge either owing to small scale upwellings, the presence of volatiles, or the combination of the two. Persistent melt near the base of the lithosphere and apparent channelization near anomaly F also suggests a role for water or other volatiles in the melts to stabilize them at relatively cool temperatures near the base of the lithosphere (Mehouachi & Singh, 2018).

Our joint seismic -MT constraints require melt fractions (> 0.01) over large swaths of the asthenosphere mantle, several hundred kilometers, and hundreds of kilometers off the ridge axis. Such high percentages are not expected to persist over time and length scales that would enable seismic imaging (Spiegelman & Elliott, 1993). Melt fractions > 0.01 could be explained by a lack of a drainage route for the melt. Melt may coalesce at a permeability boundary at the lithosphere-asthenosphere boundary, as suggested by recent numerical models that include 2-phase flow (Sim et al., 2020). Asthenospheric porosity in these models at a given snapshot in time can reach up to 10-20%, which could explain our melt fraction observations in the channels (Sim et al., 2020). The melt may also reduce the asthenospheric viscosity (Hirth & Kohlstedt, 1995; Jackson et al., 2006) potentially further promoting small scale convection. Our observations in light of these geodynamic models suggests that melt is dynamic but may be persistent on geological timescales.

Conclusions

We developed a simple relationship for shear velocity and resistivity of the oceanic lithosphere and asthenosphere that can be used to link these quantities for joint inversions based on data from the I-LAB experiments and petrophysical modelling. We used the relationship to create a shear-wave starting model that we used to re-invert the phase velocities. The new shear-wave velocity model more closely resembles the resistivity models, in particular by including a low velocity channel and also in terms of the location and shape of slow velocity anomalies. The apparent lithospheric drip was also enhanced. Overall, the correlation between the surface wave and MT data sets increased. This suggests that apparent discrepancies between the original models are more likely an artefact of resolution and inversion schemes. Surface waves cannot resolve thin channel structures unless significant prior knowledge is used in the starting model in the inversion. We also demonstrate the utility for one-sided joint inversion of resistivity and shear velocity for mantle melting and thermal structure based on petrophysical modelling. We show that shear velocity can place good constraints on melt volume, while resistivity can place good constraints on melt water content, CO_2 content or presence of sulfide melt given a simple thermal structure such as the half-space cooling model.

Our estimates of melt, melt water content and temperature are in general reasonable and within the expectations given geochemical outputs from the nearby ridge segments. The one exception is very high water or CO_2 contents (>15%) estimated in the slowest and least resistive anomalies. These high melt water or CO_2 contents could be real but would require coalescing low degree partial melts of moderately wet or carbon-rich mantle sources. Alternatively, nearly pure sulfide melts at small fractions could potentially partially explain these anomalies. Overall, joint interpretation and/or inversion of resistivity and shear velocity models holds promise for resolving debates about the lithosphere-asthenosphere system and the presence and character of partial melt in the mantle.

Acknowledgements

C. A. R., N. H. and J. M. K. were funded by the Natural Environment Research Council (NE/M003507/1 and NE/K010654/1) and the European Research Council (GA 638665). S. C. was funded by the National Science Foundation under Grant OCE−1536400 (CA−LAB). S. W. was funded by the Cecil and Ida Green Foundation and the Seafloor Electromagnetic Methods Consortium at Scripps Institution of Oceanography. Seismic data are archived at

the IRIS DMC, as 2016-2017 network XS https://doi.org/10.7914/SN/XS_2016. (Rychert et al., 2016).

Figures

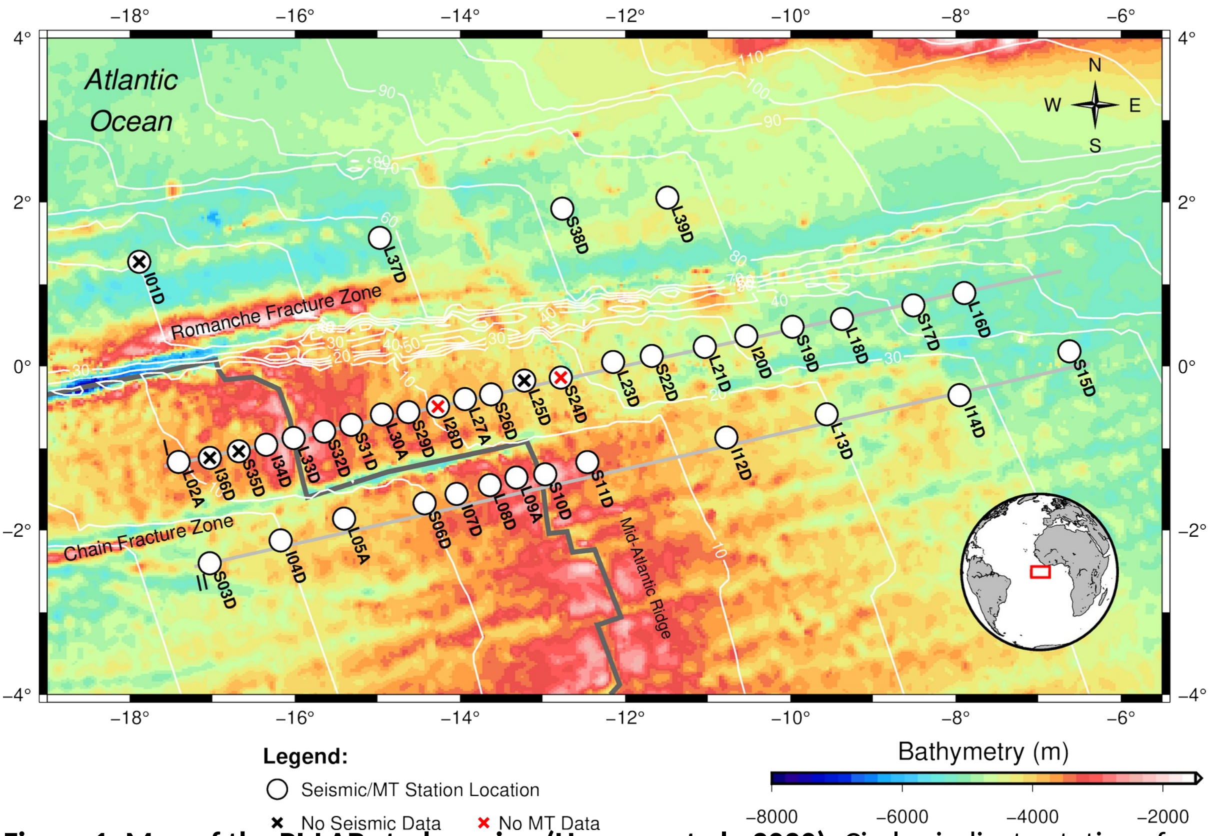

Figure 1. Map of the PI-LAB study region (Harmon et al., 2020). Circles indicate stations for seismic and MT locations with names indicated. MT stations are within 1-2 km of the seismic stations. Grey lines I and II indicate transects used in this study. Background colors indicate bathymetry (Smith & Sandwell, 1997), white contours indicate seafloor age from Seton et al., (2020), and thick, dark grey line indicates the location of the Mid-Atlantic Ridge. Red box in inset map indicates study area.

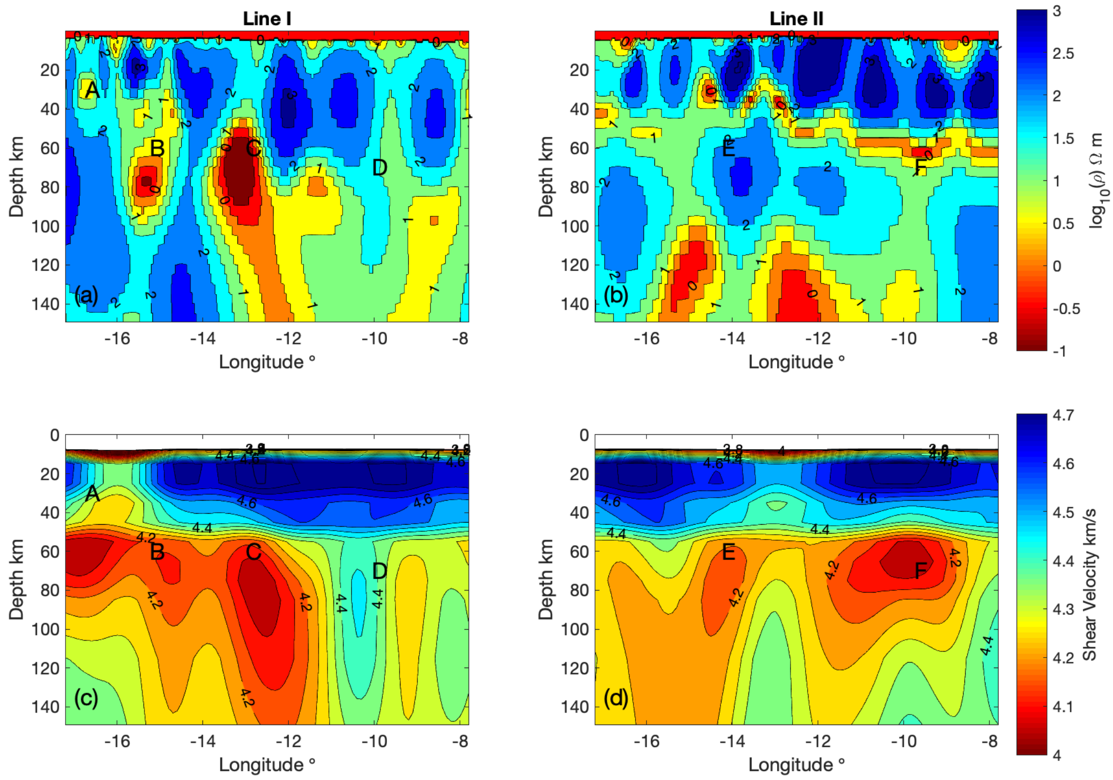

Figure 2. Resistivity model and shear-wave velocity model from previous work. Panels (a) and (b) show contoured resistivity transects from line I and line II, respectively, from Wang et al. (2020). Contour interval is 0.5 log units. Panels (c) and (d) show contoured shear velocity transects for line I and II, respectively, from Harmon et al. (2020). Contour interval is 0.05 km/s. Anomalies A, B, C, D, E and F from Harmon et al. (2020) are indicated.

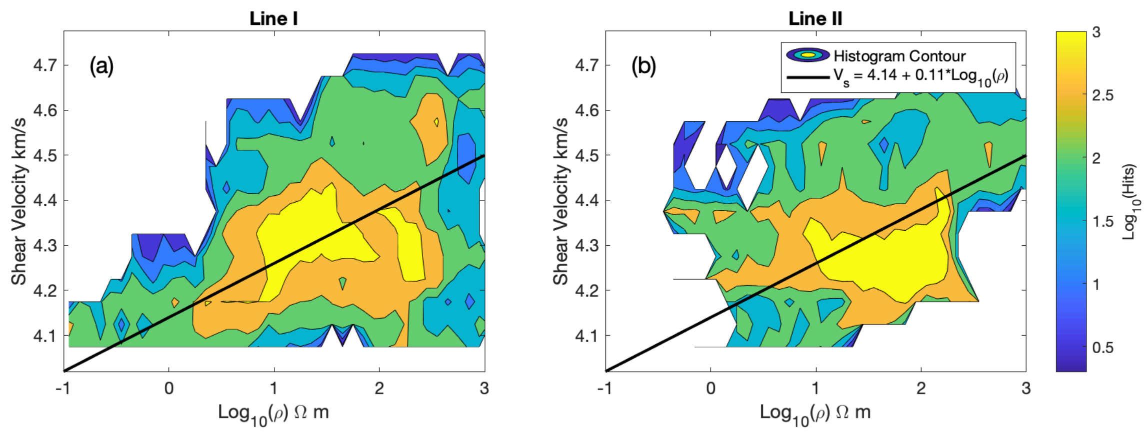

Figure 3. Cross-plot histograms of resistivity and shear-wave velocity from previous work. Panels a and b shows the histograms for line I and line II, respectively. Black line indicates preferred linear relationship from petrophysical modelling shown in Figure 4.

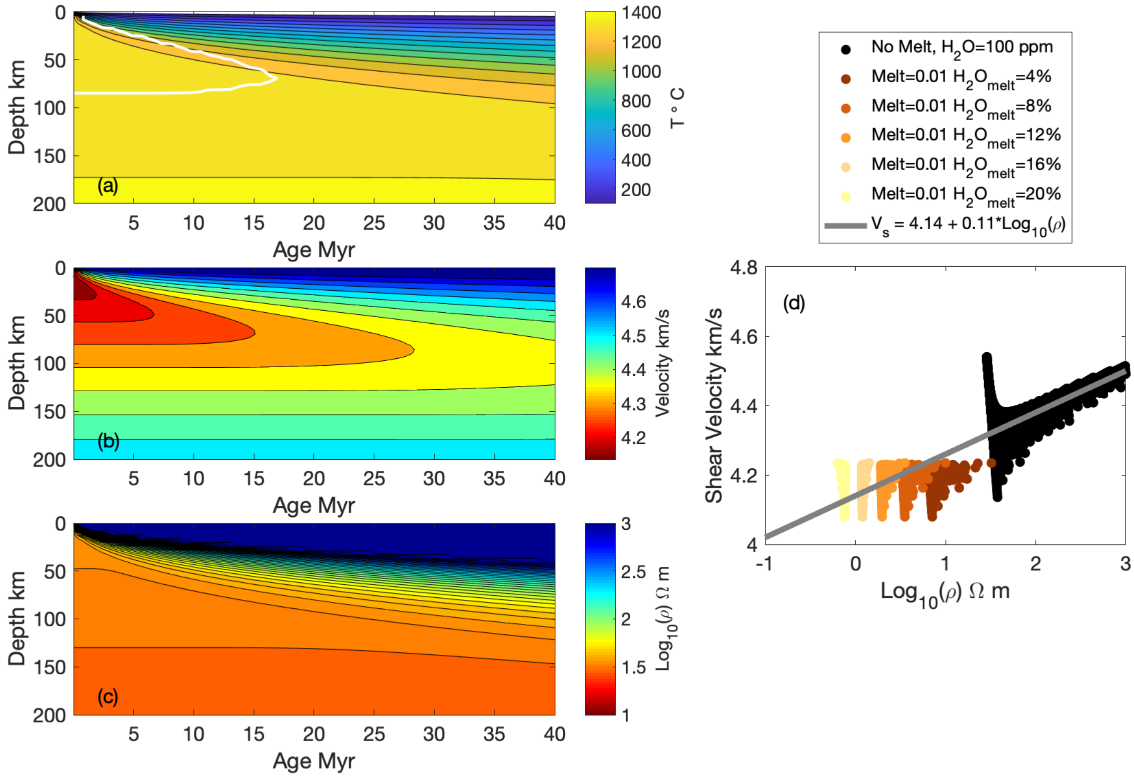

Figure 4. Petrophysical predictions for resistivity and shear-wave velocity for half-space cooling model. Panel a shows the thermal structure for the half-space cooling model, b shows the predicted shear-wave velocity structure, and c shows the predicted resistivity structure predicted from petrophysics calculated as described in the text. White line in panel a indicates the predicted melt triangle for 100 ppm water in a background mantle (Katz et al., 2003). Panel d shows the cross-plot of predicted resistivity and shear velocity without melt from panel b and c (black circles) and with a presumed melt fraction (0.01) containing different amounts of water (4-20%), within the predicted melt triangle (yellow and brown circles). Grey line in Panel d shows preferred linear relationship between resistivity and shear velocity based petrophysical modelling presented here and consistent with the cross-plot histograms presented in Figure 3.

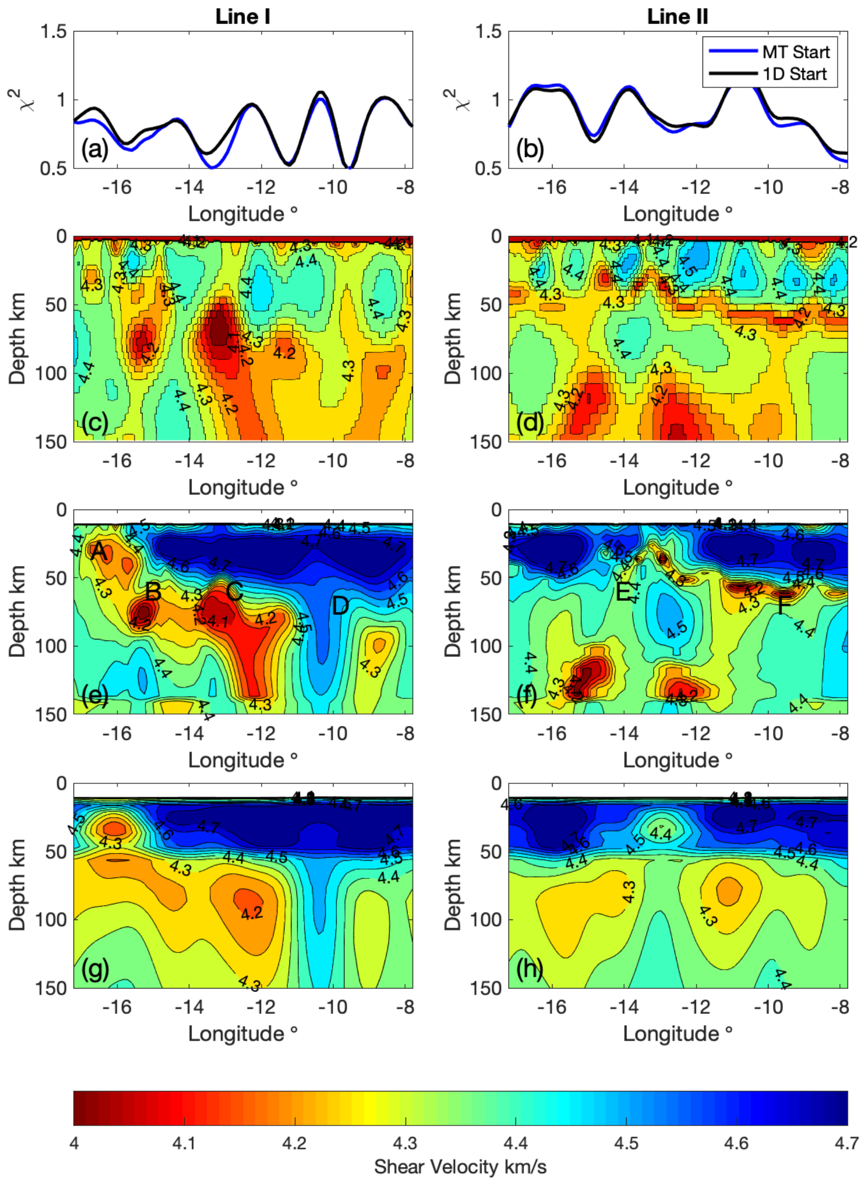

Figure 5. Shear-wave velocity inversions based on resistivity predictions. Panel a and b show misfit along line I and II using normalized chi-squared. Panel c and d show the shear-wave velocity models that result from translating the resistivity model shown in Fig. 2 to velocity using the linear relationships based on petrophysical modelling. Panels e and f show the shear-wave velocity inversion results using panels c and d, respectively, as starting models. Panels g and h the show shear velocity inversion results using the 1-D starting model from Harmon et al. (2020) and the smoothing, damping, and model parameterisation used here. Contour interval is 0.05 km/s. Asthenospheric anomalies A, B, C, D, E and F from Harmon et al. (2020) and Wang et al. (2020) are shown for reference.

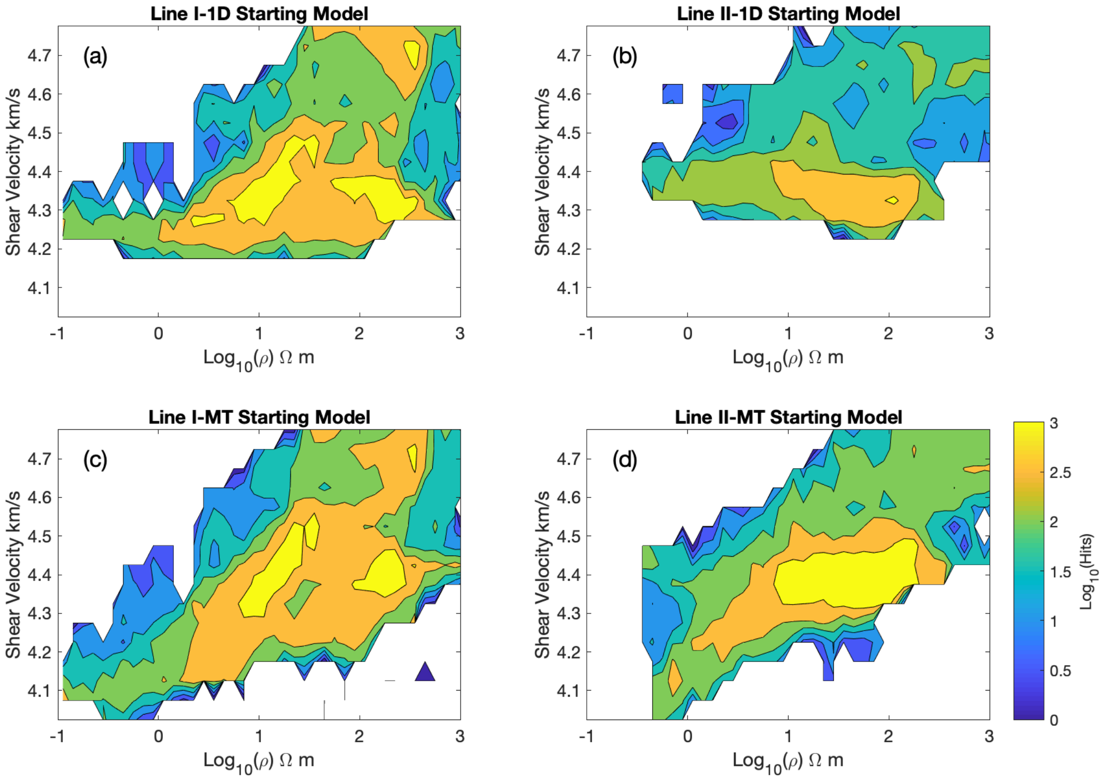

Figure 6. Cross-plot histograms of resistivity and shear-wave velocity models. Panels a and b show the cross-plot histograms for line I and line II, respectively, for the shear-wave velocity model derived from using the 1-D velocity starting model from Harmon et al. (2020) and the damping, smoothing, and parameterisation used here (Figure 5g, h). Panels c and d show the cross-plot histograms of the MT-derived shear-wave velocity model (Fig. 5 e, f).

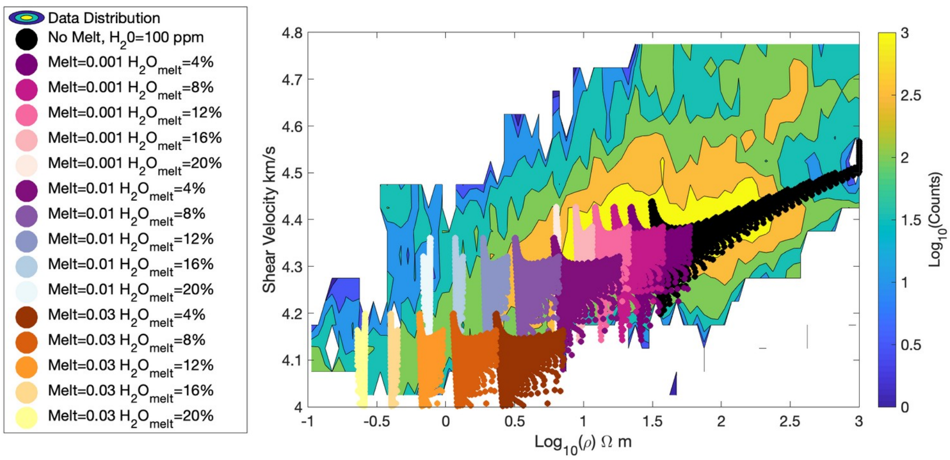

Figure 7. Cross-plot histogram of resistivity and shear-wave velocity from the MT-derived shear-wave velocity model for both lines I II and petrophysical predictions. Purely thermal predictions are shown as black dots. Colored dots show predictions for various melt fractions and melt water contents. Legend indicates the amount of imposed disequilibrium melt fraction (0.001, 0.01 and 0.03) and water content of the melt in weight % (4-20%).

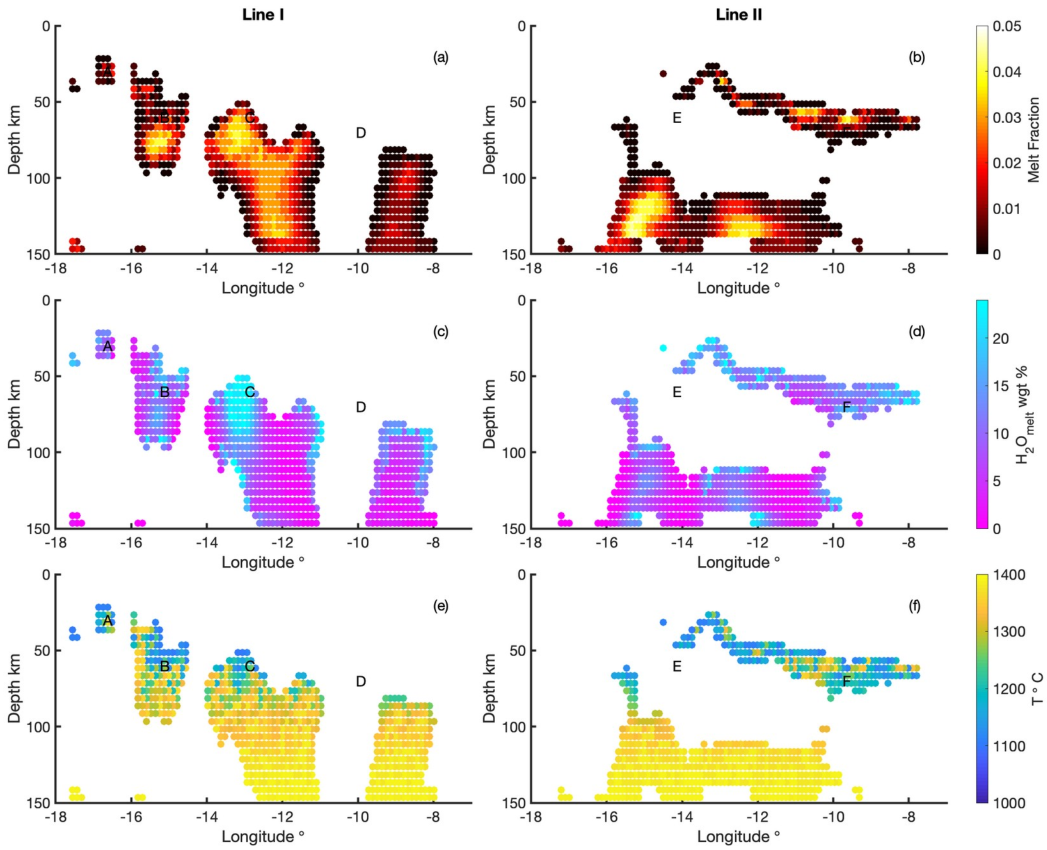

Figure 8. Results of grid search for partial melt, melt water content and mantle temperature. Panels a and b show results for partial melt fraction, panels c and d show water content of the partial melt, and panels e and f show the result for temperature for lines I and II, respectively. Anomalies A, B, C, D, E and F are plotted at the same locations as in Figure 2 for reference.

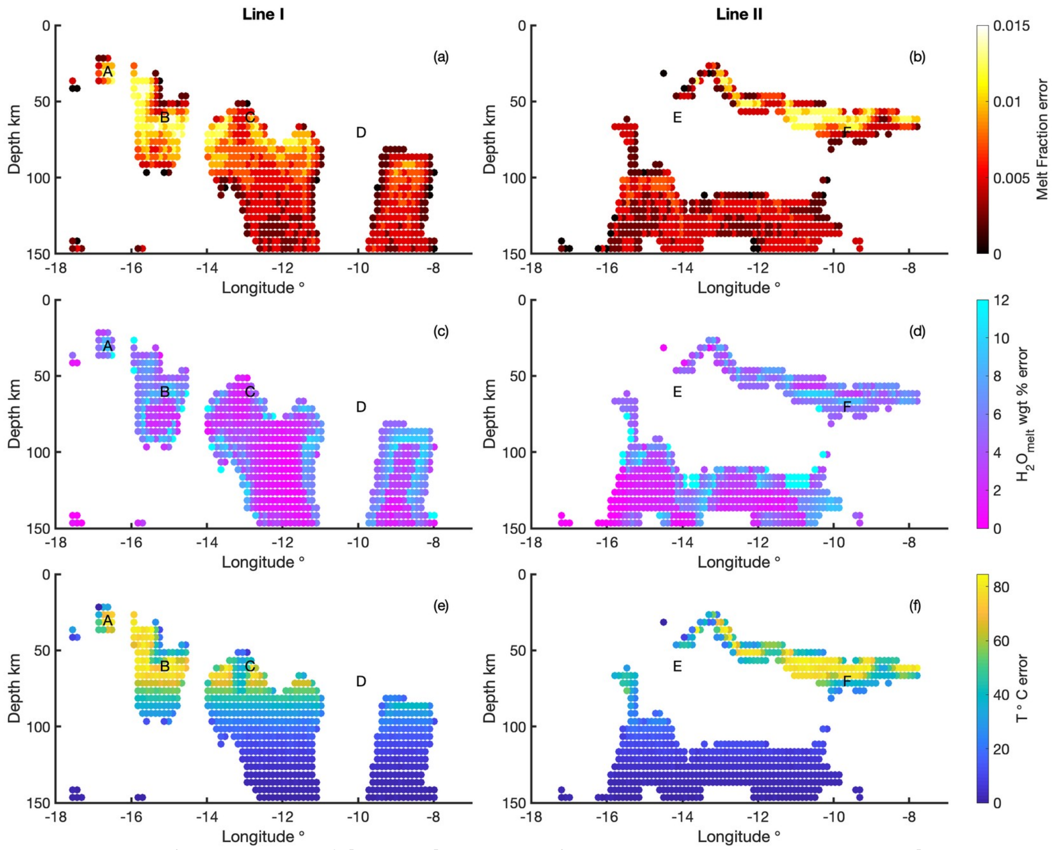

Figure 9. Error estimates of grid search for partial melt, water content of the melt and mantle temperature. Panels a and b show partial melt fraction error, panels c and d show water content of the partial melt error, and panels e and f show temperature error for line I and line II, respectively. Anomalies A, B, C, D, E and F are plotted at the same locations as in Figure 2 for reference.

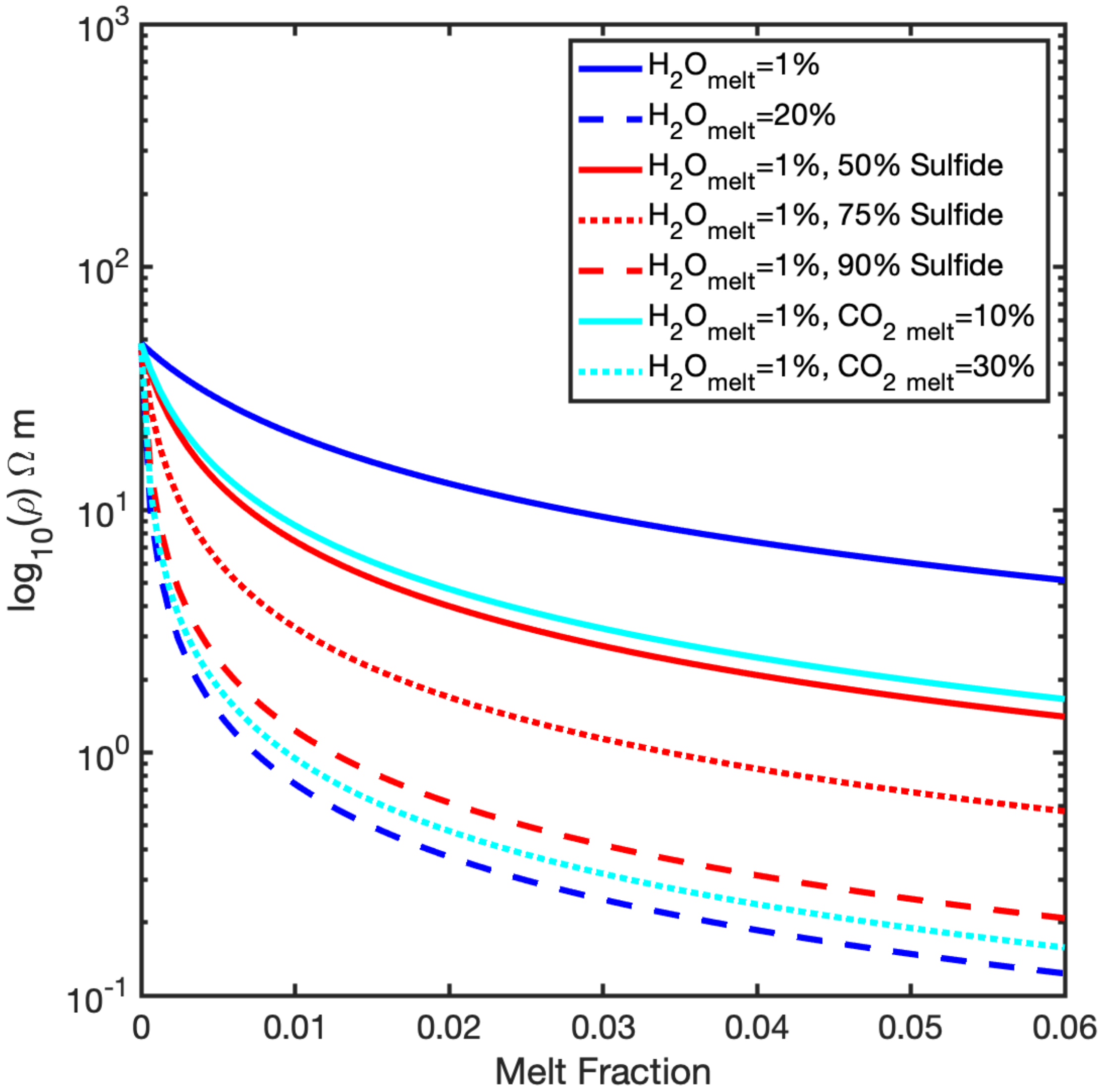

Figure 10. Effective resistivity predictions for water, CO_2 and sulfide in silicate melts as a function of melt fraction. We assume a solid mantle with 100 ppm water and disequilibrium melt at 1300°C. Legend indicates the respective water, CO_2 and sulfide concentrations. Melt with water only is shown as blue lines. Melt that includes water and CO_2 is shown as cyan lines and melt that includes water and sulfide is shown as red lines.

References

Abers, G. A., Fischer, K. M., Hirth, G., Wiens, D. A., Plank, T., Holtzman, B. K., McCarthy, C., & Gazel, E. (2014, Sep). Reconciling mantle attenuation-temperature relationships from seismology, petrology, and laboratory measurements. *Geochemistry Geophysics Geosystems*, *15*(9), 3521-3542. https://doi.org/10.1002/2014gc005444

Agius, M., Harmon, N., Rychert, C. A., Tharimena, S., & Kendall, J. M. (2018). Sediment Characterization at the Equatorial Mid−Atlantic Ridge From P−to−S Teleseismic Phase Conversions Recorded on the PI−LAB Experiment. *Geophysical Research Letters*, *45*. https://doi.org/https://doi.org/10.1029/2018GL080565

Anderson, D., & Sammis, C. (1970). Partial Melting in the Upper Mantle. *Phys. Earth Plan. Interiors*, *3*, 41-50.

Baba, K., Chave, A. D., Evans, R. L., Hirth, G., & Mackie, R. L. (2006, Feb 17). Mantle dynamics beneath the East Pacific Rise at 17 degrees S: Insights from the Mantle Electromagnetic and Tomography (MELT) experiment. *J. Geophys. Res.*, *111*(B02101). https://doi.org/doi:10.1029/2004JB003598

Bell, S., Ruan, Y. Y., & Forsyth, D. W. (2016, Oct). Ridge asymmetry and deep aqueous alteration at the trench observed from Rayleigh wave tomography of the Juan de Fuca plate. *Journal of Geophysical Research-Solid Earth*, *121*(10), 7298-7321. https://doi.org/10.1002/2016jb012990

Bennington, N. L., Zhang, H. J., Thurber, C. H., & Bedrosian, P. A. (2015, May). Joint Inversion of Seismic and Magnetotelluric Data in the Parkfield Region of California Using the Normalized Cross-Gradient Constraint. *Pure and Applied Geophysics*, *172*(5), 1033-1052. https://doi.org/10.1007/s00024-014-1002-9

Clark, A. N., & Lesher, C. E. (2017, Dec). Elastic properties of silicate melts: Implications for low velocity zones at the lithosphere-asthenosphere boundary. *Science Advances*, *3*(12). <Go to ISI>://WOS:000418003100012

Dasgupta, R., & Hirschmann, M. M. (2010, Sep 15). The deep carbon cycle and melting in Earth's interior. *Earth and Planetary Science Letters*, *298*(1-2), 1-13. https://doi.org/10.1016/j.epsl.2010.06.039

Ducea, M. N., & Park, S. K. (2000). Enhanced Mantle Conductivity from Sulfide Minerals, Southern Sierra Nevada, California. *Geophysical Research Letters*, *27*(16), 2405-2408. https://doi.org/https://doi.org/10.1029/2000GL011565

Dunn, R. A., & Forsyth, D. W. (2003, Jul 30). Imaging the transition between the region of mantle melt generation and the crustal magma chamber beneath the southern East Pacific Rise with short-period Love waves. *J. Geophys. Res.*, *108*(B7), 2352, doi:2310.1029/2002JB002217. <Go to ISI>://000184708700002

Dziewonski, A. M., & Anderson, D. L. (1981). Preliminary Reference Earth Model. *Phys. Earth Plan. Inter.*, *25*(4), 297-356. <Go to ISI>://A1981LV59500002

Evans, R. L., Tarits, P., Chave, A. D., White, A., Heinson, G., Filloux, J. H., Toh, H., Seama, N., Utada, H., Booker, J. R., & Unsworth, M. J. (1999). Asymmetric electrical structure in the mantle beneath the East Pacific Rise at 17 degrees S. *Science*, *286*(5440), 752-756.

Forsyth, D. W., & Li, A. (2005). Array-analysis of two-dimensional variations in surface wave phase velocity and azimuthal anisotropy in the presence of multipathing interference. In A. Levander & G. Nolet (Eds.), *Seismic Data Analysis and Imaging with Global and Local Arrays*. AGU Monograph.

Forsyth, D. W., Scheirer, D. S., Webb, S. C., Dorman, L. M., Orcutt, J. A., Harding, A. J., Blackman, D. K., Morgan, J. P., Detrick, R. S., Shen, Y., Wolfe, C. J., Canales, J. P., Toomey, D. R., Sheehan, A. F., Solomon, S. C., Wilcock, W. S. D., & Team, M. S. (1998, May 22). Imaging the deep seismic structure beneath a mid-ocean ridge: The MELT experiment. *Science*, *280*(5367), 1215-1218. <Go to ISI>://000073852500033

Frost, B. R., Fyfe, W. S., Tazaki, K., & Chan, T. (1989, Jul 13). Grain-Boundary Graphite in Rocks and Implications for High Electrical-Conductivity in the Lower Crust. *Nature*, *340*(6229), 134-136. https://doi.org/DOI 10.1038/340134a0

Gaherty, J. B., Jordan, T. H., & Gee, L. S. (1996). Seismic structure of the upper mantle in a central Pacific corridor. *J. Geophys. Res.*, *101*(B10), 22,291-222,309.

Gallardo, L. A., & Meju, M. A. (2004, Mar 27). Joint two-dimensional DC resistivity and seismic travel time inversion with cross-gradients constraints. *Journal of Geophysical Research-Solid Earth*, *109*(B3). https://doi.org/Artn B03311
10.1029/2003jb002716

Gao, H. Y. (2016, May 28). Seismic velocity structure of the Juan de Fuca and Gorda plates revealed by a joint inversion of ambient noise and regional earthquakes. *Geophysical Research Letters*, *43*(10), 5194-5201. https://doi.org/10.1002/2016gl069381

Gardés, E., Gaillard, F., & Tarits, P. (2014). Toward a unified hydrous olivine electrical conductivity law. *Geochemistry, Geophysics, Geosystems*, *15*(12), 4984-5000. https://doi.org/https://doi.org/10.1002/2014GC005496

Goetze, C., Poirier, J. P., Kelly, A., Cook, A. H., & Greenwood, G. W. (1978). The mechanisms of creep in olivine. *Philosophical Transactions of the Royal Society of London. Series A, Mathematical and Physical Sciences*, *288*(1350), 99-119. https://doi.org/doi:10.1098/rsta.1978.0008

Haber, E., & Oldenburg, D. (1997, 1997/02/01). Joint inversion: a structural approach. *Inverse Problems*, *13*(1), 63-77. https://doi.org/10.1088/0266-5611/13/1/006

Hacker, B. R., & Abers, G. A. (2004, Jan 20). Subduction Factory 3: An Excel worksheet and macro for calculating the densities, seismic wave speeds, and H2O contents of minerals and rocks at pressure and temperature. *Geochemistry Geophysics Geosystems*, *5*. https://doi.org/Artn Q01005
10.1029/2003gc000614

Hammond, W. C., & Humphreys, E. D. (2000, May 10). Upper mantle seismic wave velocity: Effects of realistic partial melt geometries. *J. Geophys. Res.*, *105*(5), 10975-10986. <Go to ISI>://000087027400012

Harmon, N., Rychert, C., Kendall, J., Tharimena, S., Bogiatzis, P., & Agius, M. (2020). Evolution of the oceanic Lithosphere in the equatorial Atlantic from Rayleigh Wave tomography, evidence for small-scale convection from the PI-LAB experiment. *Geochem. Geophys. Geosys.*(10.1029/2020GC009174). https://doi.org/10.1029/2020GC009174

Harmon, N., Rychert, C. A., Agius, M. R., Tharimena, S., Le Bas, T. P., Kendall, J. M., & Constable, S. (2018). Marine geophysical investigation of the Chain Fracture Zone in the equatorial Atlantic from the PI-LAB Experiment. *J. Geophys. Res.*, *123*, 11,016–011,030. https://doi.org/10.1029/2018JB015982

Harmon, N., Rychert, C. A., Kendall, J. M., Agius, M., Bogiatzis, P., & Tharimena, S. (2020, Sep). Evolution of the Oceanic Lithosphere in the Equatorial Atlantic From Rayleigh Wave Tomography, Evidence for Small-Scale Convection From the PI-LAB Experiment. *Geochemistry Geophysics Geosystems*, *21*(9). https://doi.org/ARTN e2020GC009174
10.1029/2020GC009174

Havlin, C., Holtzman, B., & Hopper, E. (2021, 2021/02/16/). Inference of thermodynamic state in the asthenosphere from anelastic properties, with applications to north American upper mantle. *Phys. Earth Plan. Inter.*, 106639. https://doi.org/https://doi.org/10.1016/j.pepi.2020.106639

Helffrich, G., Kendall, J.-M., Hammond, J. O. S., & Carroll, M. R. (2011). Sulfide melts and long-term low seismic wavespeeds in lithospheric and asthenospheric mantle. *Geophysical Research Letters*, *38*(11). https://doi.org/https://doi.org/10.1029/2011GL047126

Herrmann, R. B. (2013, Nov-Dec). Computer Programs in Seismology: An Evolving Tool for Instruction and Research. *Seismological Research Letters*, *84*(6), 1081-1088. https://doi.org/10.1785/0220110096

Hirschmann, M. M. (2010, Mar). Partial melt in the oceanic low velocity zone. *Phys. Earth Planet. Inter.*, *179*(1-2), 60-71. https://doi.org/10.1016/J.Pepi.2009.12.003

Hirth, G., & Kohlstedt, D. L. (1995, Aug 10). Experimental Constraints on the Dynamics of the Partially Molten Upper-Mantle .2. Deformation in the Dislocation Creep Regime. *J. Geophys. Res.*, *100*(8), 15441-15449. <Go to ISI>://A1995RN99200034

Jackson, I., & Faul, U. H. (2010, Nov). Grainsize-sensitive viscoelastic relaxation in olivine: Towards a robust laboratory-based model for seismological application. *Phys. Earth Plan. Inter.*, *183*(1-2), 151-163. https://doi.org/Doi 10.1016/J.Pepi.2010.09.005

Jackson, I., Faul, U. H., Fitz Gerald, J. D., & Morris, S. J. S. (2006, Dec 20). Contrasting viscoelastic behavior of melt-free and melt-bearing olivine: Implications for the nature of grain-boundary sliding. *Materials Science and Engineering a-Structural Materials Properties Microstructure and Processing*, *442*(1-2), 170-174. https://doi.org/Doi 10.1016/J.Msea.2006.01.136

Jegen, M. D., Hobbs, R. W., Tarits, P., & Chave, A. (2009, 2009/05/30/). Joint inversion of marine magnetotelluric and gravity data incorporating seismic constraints: Preliminary results of sub-basalt imaging off the Faroe Shelf. *Earth and Planetary Science Letters*, *282*(1), 47-55. https://doi.org/https://doi.org/10.1016/j.epsl.2009.02.018

Johansen, S. E., Panzner, M., Mittet, R., Amundsen, H. E. F., Lim, A., Vik, E., Landro, M., & Arntsen, B. (2019, Mar 21). Deep electrical imaging of the ultraslow-spreading Mohns Ridge. *Nature*, *567*(7748), 379-+. https://doi.org/10.1038/s41586-019-1010-0

Karato, S.-I. (2012). On the origin of the asthenosphere. *Earth Planet. Sci. Lett.*, *321-322*, 95-103. (10.1016/j.epsl.2012.01.001)

Katz, R. F., Spiegelman, M., & Langmuir, C. H. (2003, Sep 9). A new parameterization of hydrous mantle melting. *Geochem. Geophys. Geosys.*, *4*(9), 1073, doi:1010.1029/2002GC000433. <Go to ISI>://000189015400002

Kawakatsu, H., Kumar, P., Takei, Y., Shinohara, M., Kanazawa, T., Araki, E., & Suyehiro, K. (2009, Apr 24). Seismic Evidence for Sharp Lithosphere-Asthenosphere Boundaries of Oceanic Plates. *Science*, *324*(5926), 499-502. https://doi.org/10.1126/science.1169499

Key, K. (2016, Oct). MARE2DEM: a 2-D inversion code for controlled-source electromagnetic and magnetotelluric data. *Geophys. J. Int.*, *207*(1), 571-588. https://doi.org/10.1093/gji/ggw290

Key, K., Constable, S., Liu, L., & Pommier, A. (2013, 28 March). Electical image of passive mantel upwelling beneath the northern East Pacific Rise. *Nature*, *495*, 499-502. https://doi.org/doi:10.1038/nature11932

Le Voyer, M., Cottrell, E., Kelley, K. A., Brounce, M., & Hauri, E. H. (2015, Jan). The effect of primary versus secondary processes on the volatile content of MORB glasses: An example from the equatorial Mid-Atlantic Ridge (5 degrees N-3 degrees S). *Journal of*

Geophysical Research-Solid Earth, *120*(1), 125-144. https://doi.org/10.1002/2014jb011160

Le Voyer, M., Hauri, E. H., Cottrell, E., Kelley, K. A., Salters, V. J. M., Langmuir, C. H., Hilton, D. R., Barry, P. H., & Füri, E. (2019). Carbon Fluxes and Primary Magma CO2 Contents Along the Global Mid-Ocean Ridge System. *Geochemistry, Geophysics, Geosystems*, *20*(3), 1387-1424. https://doi.org/https://doi.org/10.1029/2018GC007630

McKenzie, D., & Parker, R. (1967). The North Pacific: an Example of Tectonics on a Sphere. *Nature*, *216*, 1276–1280 https://doi.org/https://doi.org/10.1038/2161276a0

Mehouachi, F., & Singh, S. (2018). Water-rich sublithospheric melt channel in the equatorial Atlantic Ocean. *Nat. Geosci.*, *11*, 65-69. https://doi.org/doi:10.1038/s41561-017-0034-z

Moorkamp, M., Heincke, B., Jegen, M., Roberts, A. W., & Hobbs, R. W. (2011, Jan). A framework for 3-D joint inversion of MT, gravity and seismic refraction data. *Geophys. J. Int.*, *184*(1), 477-493. https://doi.org/10.1111/j.1365-246X.2010.04856.x

Moorkamp, M., Jones, A. G., & Fishwick, S. (2010, Apr 30). Joint inversion of receiver functions, surface wave dispersion, and magnetotelluric data. *Journal of Geophysical Research-Solid Earth*, *115*. https://doi.org/Artn B04318
10.1029/2009jb006369

Naif, S., Key, K., Constable, S., & Evans, R. L. (2013, Mar 21). Melt-rich channel observed at the lithosphere-asthenosphere boundary. *Nature*, *495*(7441), 356-359. <Go to ISI>://WOS:000316650500040

Naif, S., Selway, K., Murphy, B. S., Egbert, G., & Pommier, A. (2021, 2021/04/01/). Electrical conductivity of the lithosphere-asthenosphere system. *Phys. Earth Plan. Inter.*, *313*, 106661. https://doi.org/https://doi.org/10.1016/j.pepi.2021.106661

Ni, H., Keppler, H., & Behrens, H. (2011, 2011/09/01). Electrical conductivity of hydrous basaltic melts: implications for partial melting in the upper mantle. *Contributions to Mineralogy and Petrology*, *162*(3), 637-650. https://doi.org/10.1007/s00410-011-0617-4

Parker, R. L., & Oldenburg, D. W. (1973). Thermal Model of Ocean Ridges. *Nature, Phys. Sci.*, *242*(122), 137-139. <Go to ISI>://A1973P472600005

Priestley, K., & McKenzie, D. (2006, Apr 15). The thermal structure of the lithosphere from shear wave velocities. *Earth Plan. Sci. Lett.*, *244*(1-2), 285-301. <Go to ISI>://000236991300019

Rychert, C., Harmon, N., Constable, S., Kendall, J., Tharimena, S., Wang, S., Bogiatzis, P., Agius, M., Schlaphorst, D., & Hicks, S. (2019). *A dynamic lithosphere-asthenosphere boundary dictated by variations in melt generation and migration: Results from the*

PI-LAB Experiment in the Equatorial Mid Atlantic American Geophysical Union, San Francisco, CA, USA.

Rychert, C. A., Fischer, K. M., & Rondenay, S. (2005, Jul 28). A sharp lithosphere-asthenosphere boundary imaged beneath eastern North America. *Nature*, *436*(7050), 542-545. <Go to ISI>://000230788800058

Rychert, C. A., & Harmon, N. (2017). Constraints on the anisotropic contributions to velocity discontinuities at ~60 km depth beneath the Pacific. *Geochemistry, Geophysics, Geosystems*, *18*. https://doi.org/10.1002/2017GC006850

Rychert, C. A., Harmon, N., Constable, S., & Wang, S. G. (2020, Oct). The Nature of the Lithosphere-Asthenosphere Boundary. *Journal of Geophysical Research-Solid Earth*, *125*(10). https://doi.org/ARTN e2018JB016463 10.1029/2018JB016463

Rychert, C. A., Harmon, N., & Tharimena, S. (2018). Seismic Imaging of the Base of the Ocean Plates. In H. Yuan (Ed.), *Lithospheric Discontinuities* (pp. 71-87). AGU Monographs. https://doi.org/accepted

Rychert, C. A., Kendall, J. M., & Harmon, N. (2016). *Passive Imaging of the Lithosphere-Asthenosphere Boundary*. https://doi.org/ https://doi.org/10.7914/SN/XS_2016

Rychert, C. A., Rondenay, S., & Fischer, K. M. (2007, Aug 25). P-to-S and S-to-P imaging of a sharp lithosphere-asthenosphere boundary beneath eastern North America. *Journal of Geophysical Research-Solid Earth*, *112*(B8). https://doi.org/Artn B08314 10.1029/2006jb004619

Rychert, C. A., & Shearer, P. (2011). Imaging the lithosphere-asthenosphere boundary beneath the Pacific using SS waveform modeling. *J. Geophys. Res.*, *116*(7), B07307, doi:07310.01029/02010JB008070.

Rychert, C. A., & Shearer, P. M. (2009, Apr 24). A Global View of the Lithosphere-Asthenosphere Boundary. *Science*, *324*(5926), 495-498. https://doi.org/Doi 10.1126/Science.1169754

Rychert, C. A., Tharimena, S., Harmon, N., Wang, S., Constable, C. G., Kendall, J. M., Bogiatzis, P., Agius, M., & Schlaphorst, D. (2021). A dynamic Lithosphere Asthenosphere Boundary near the Equatorial Mid-Atlantic Ridge. *Earth & Planet. Sci. Let.*(Submitted).

Saikia, U., Rychert, C., Harmon, N., & Kendall, J. M. (2021). Upper Mantle Anisotropic Shear Velocity Structure at the Equatorial Mid-Atlantic Ridge Constrained by Rayleigh Wave Group Velocity Analysis From the PI-LAB Experiment. *Geochemistry, Geophysics, Geosystems*, *22*(3), e2020GC009495. https://doi.org/https://doi.org/10.1029/2020GC009495

Schmeling, H. (1985, Dec 1). Numerical-Models on the Influence of Partial Melt on Elastic, Anelastic and Electric Properties of Rocks .1. Elasticity and Anelasticity. *Phys. Earth Plan. Inter.*, *41*(1), 34-57. https://doi.org/Doi 10.1016/0031-9201(85)90100-1

Schutt, D. L., & Lesher, C. E. (2006, May 2). Effects of melt depletion on the density and seismic velocity of garnet and spinel lherzolite. *Journal of Geophysical Research-Solid Earth*, *111*(B5), doi:10.1029/2003JB002950. https://doi.org/Artn B05401
Doi 10.1029/2003jb002950

Seton, M., Müller, R. D., Zahirovic, S., Williams, S., Wright, N. M., Cannon, J., Whittaker, J. M., Matthews, K. J., & McGirr, R. (2020). A Global Data Set of Present-Day Oceanic Crustal Age and Seafloor Spreading Parameters. *Geochemistry, Geophysics, Geosystems*, *21*(10), e2020GC009214. https://doi.org/https://doi.org/10.1029/2020GC009214

Sifre, D., Gardes, E., Massuyeau, M., Hashim, L., Hier-Majumder, S., & Gaillard, F. (2014, May 1). Electrical conductivity during incipient melting in the oceanic low-velocity zone. *Nature*, *509*(7498), 81-+. https://doi.org/10.1038/nature13245

Sim, S. J., Spiegelman, M., Stegman, D. R., & Wilson, C. (2020, Jul). The influence of spreading rate and permeability on melt focusing beneath mid-ocean ridges. *Phys. Earth Plan. Inter.*, *304*. https://doi.org/ARTN 106486
10.1016/j.pepi.2020.106486

Smith, W. H. F., & Sandwell, D. T. (1997). Global seafloor topography from satellite altimetry and ship soundings. *Science*, *277*, 1957-1962.

Spiegelman, M., & Elliott, T. (1993, 1993/07/01/). Consequences of melt transport for uranium series disequilibrium in young lavas. *Earth and Planetary Science Letters*, *118*(1), 1-20. https://doi.org/https://doi.org/10.1016/0012-821X(93)90155-3

Stern, T. A., Henrys, S. A., Okaya, D., Louie, J. N., Savage, M. K., Lamb, S., Sato, H., Sutherland, R., & Iwasaki, T. (2015, Feb 5). A seismic reflection image for the base of a tectonic plate. *Nature*, *518*(7537), 85-+. https://doi.org/10.1038/nature14146

Stesky, R. M., & Brace, W. F. (1973). Electrical Conductivity of Serpentinized Rocks to 6 Kilobars. *Journal of Geophysical Research*, *78*(32), 7614-7621. https://doi.org/DOI 10.1029/JB078i032p07614

Stixrude, L., & Lithgow-Bertelloni, C. (2005, Mar 15). Mineralogy and elasticity of the oceanic upper mantle: Origin of the low-velocity zone. *J. Geophys. Res.*, *110*, B03204, 03210.01029/02004JB002965. <Go to ISI>://000227876300002

Takei, Y. (1998). Constitutive mechanical relations of solid-liquid composites in terms of grain-boundary contiguity. *Journal of Geophysical Research: Solid Earth*, *103*(B8), 18183-18203. https://doi.org/https://doi.org/10.1029/98JB01489

Tan, Y., & Helmberger, D. V. (2007, Aug 1). Trans-Pacific upper mantle shear velocity structure. *J. Geophys. Res.*, *112*(8), B08301, doi:08310.01029/02006JB004853. <Go to ISI>://000248604300007

Tharimena, S., Rychert, C., Harmon, N., & White, P. (2017). Imaging Pacific lithosphere seismic discontinuities—Insights from SS precursor modeling. *Journal of Geophysical Research: Solid Earth*, n/a-n/a. https://doi.org/10.1002/2016JB013526

Wang, S., Constable, S., Reyes-Ortega, V., Jahandari, H., Farquharson, C., & Esquivel, T. A. (2021). Two-dimensional determinant inversion of marine magnetotelluric data and a field example from the Gulf of California, Mexico. *Geophysics*, *86*(1), E37-E57. https://doi.org/10.1190/geo2019-0735.1

Wang, S. G., Constable, S., Reyes-Ortega, V., & Rychert, C. A. (2019, Aug). A newly distinguished marine magnetotelluric coast effect sensitive to the lithosphere-asthenosphere boundary. *Geophys. J. Int.*, *218*(2), 978-987. https://doi.org/10.1093/gji/ggz202

Wang, S. G., Constable, S., Rychert, C. A., & Harmon, N. (2020, Sep). A Lithosphere-Asthenosphere Boundary and Partial Melt Estimated Using Marine Magnetotelluric Data at the Central Middle Atlantic Ridge. *Geochemistry Geophysics Geosystems*, *21*(9). https://doi.org/ARTN e2020GC009177
10.1029/2020GC009177

Workman, R. K., & Hart, S. R. (2005, Feb 28). Major and trace element composition of the depleted MORB mantle (DMM). *Earth and Planetary Science Letters*, *231*(1-2), 53-72. https://doi.org/10.1016/j.epsl.2004.12.005

Yamauchi, H., & Takei, Y. (2016, Nov). Polycrystal anelasticity at near-solidus temperatures. *Journal of Geophysical Research*, *121*(11), 7790-7820. https://doi.org/10.1002/2016jb013316